Microsyst Technol (2009) 15:581–593
DOI 10.1007/s00542-008-0760-7

TECHNICAL PAPER

Numerical analyses of peel demolding for UV embossing of high aspect ratio micro-patterning

L. P. Yeo · S. C. Joshi · Y. C. Lam · Mary B. Chan-Park · D. E. Hardt

Received: 8 September 2008 / Accepted: 5 December 2008 / Published online: 13 January 2009

Abstract Ultraviolet (UV) embossing, involving molding against micro-structured molds, is a quick and efficient method to mass produce high aspect ratio micro-features. A crucial challenge to the repeatability and large-scale application of this technique is successful demolding, which escalates in difficulty with increasing aspect ratio, due to increased polymer-mold mechanical interlocking. Some of the key factors affecting UV embossing include the crosslinked polymer shrinkage and material properties, interfacial strength between polymer to mold and the de-molding method. This paper presents a new method to simulate the demolding of UV cured polymer from a nickel mold. Hyperelastic material model and rate-independent cohesive zone modeling were employed in the numerical simulation; linear elastic polymer response, although relatively easy to apply, was not adequate. Progressive shrinkage was implemented, leading to delamination of the polymer-mold interface. The subsequent peeling of the cured polymer from the mold was modeled with increasing prescribed displacement**.** The optimal shrinkage degree was found to increase from 0.92 to 1.9% with increasing mold aspect ratio (aspect ratio is defined as height to width ratio) from 5 to 10.

L. P. Yeo · Y. C. Lam (✉) · M. B. Chan-Park · D. E. Hardt
Singapore-MIT Alliance, N2-B2C-15, Nanyang Technological University, 50 Nanyang Avenue, Singapore 639798, Singapore
e-mail: myclam@ntu.edu.sg

L. P. Yeo
Singapore Institute of Manufacturing Technology (SIMTech), 71 Nanyang Drive, Singapore 638075, Singapore

S. C. Joshi · Y. C. Lam
School of Mechanical and Aerospace Engineering, Nanyang Technological University, 50 Nanyang Avenue, Singapore 639798, Singapore

M. B. Chan-Park
School of Chemical and Biomedical Engineering, Nanyang Technological University, 50 Nanyang Avenue, Singapore 639798, Singapore

D. E. Hardt
Department of Mechanical Engineering, Massachusetts Institute of Technology, Cambridge, MA 02139-430, USA

1 Introduction

Polymeric high aspect ratio micro-arrays have important applications in the field of microlenses (Gale 1997), tissue engineering (Anderson et al. 2005), liquid crystal displays and microfluidics (Unger et al. 2000). UV embossing (Shvartsman 1991; Bender et al. 2000; Otto et al. 2001; Gao et al. 2004) is a replication technique that requires only low-temperature and low-pressure molding conditions, is compatible with high-throughput/short time cycle processing and provides good dimensional fidelity. In this process (Fig. 1a–d), a multifunctional thermoset acrylate pre-polymer resin is dispensed onto a microstructured mold, covered with a thin substrate film to reduce oxygen inhibition prior to photo-polymerization, and hardened with UV radiation. The polymer typically shrinks somewhat in the hardening or curing process. After UV curing, the polymer and substrate film are peeled from the mold (Chan-Park and Neo 2003; Chan-Park et al. 2003c). To realize the good dimension replication that a UV embossing mold can in principle produce and to keep the mold free of residue for the next use, the embossings must demold fully from the mold.

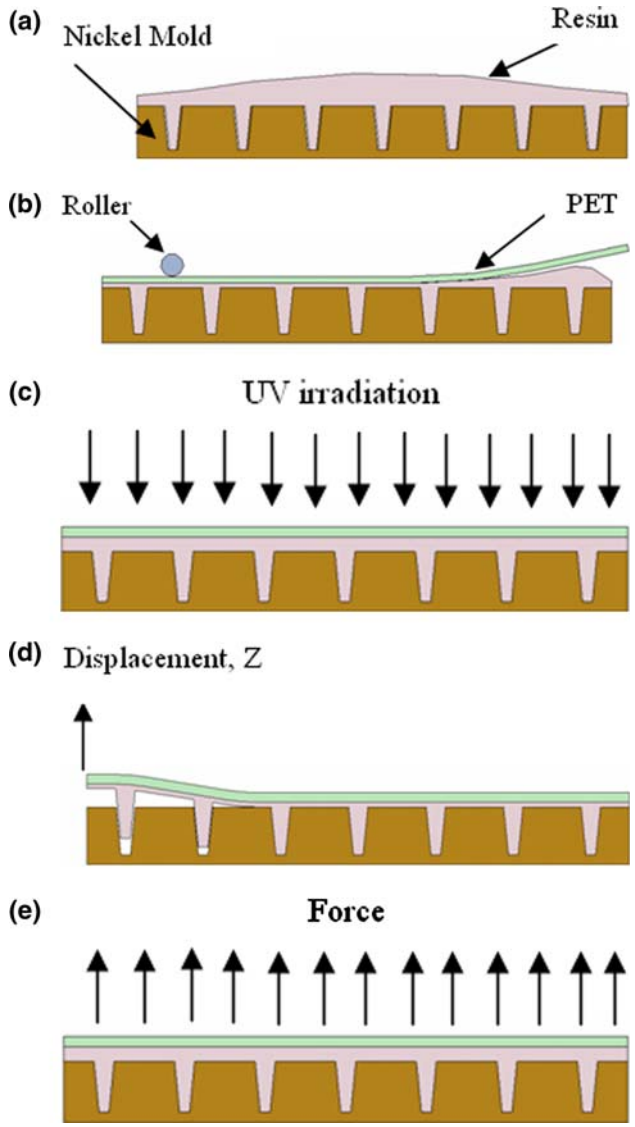

Fig. 1 UV embossing process sequence: **a** Dispensing of resin, **b** Placement of Melinex film, **c** UV exposure, **d** Peel demolding with applied displacement Z, **e** Parallel demolding

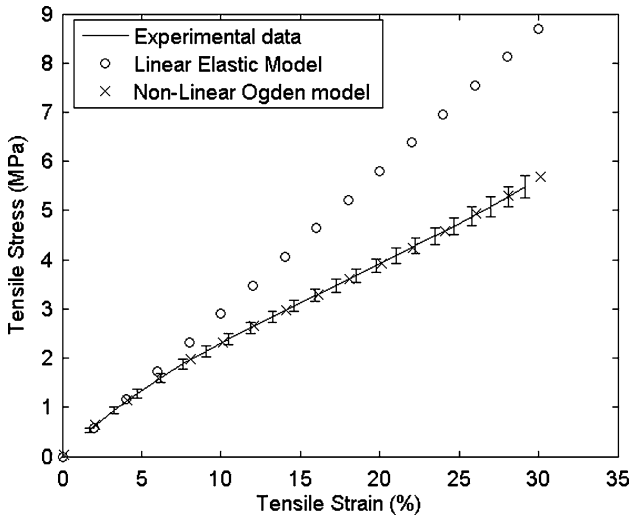

Fig. 2 Stress–strain in experimental PUR compound: averaged tensile stress–strain data and non-linear Ogden and linear elastic models. The error bars denote one standard deviation from the experimental mean data. The largest tangent modulus (29 MPa) was used for the linear elastic model

Demolding has been identified as a key challenge in high aspect ratio polymeric micro-patterning. Parameters that affect demolding in UV embossing include UV exposure time and intensity, which have a direct relation to shrinkage, the properties of the mold/polymer interface (Gao et al. 2006) and the elastic modulus and ultimate tensile strength (UTS) of the polymer.

Numerical analysis using Cohesive Zone Modeling (CZM) (Xu and Needleman 1994; Rahulkumar et al. 1999; Rahulkumar et al. 2000; Cornec et al. 2003) to determine fracture behavior between two dissimilar materials has been used extensively in recent years. Preliminary analyses using CZM to predict the success or failure of demolding from microstructured high aspect ratio molds for polymeric micro-arrays was first reported by our group (Chan-Park et al. 2003b). Parallel demolding with force control (Fig. 1e) for molds with an aspect ratio of 5 was investigated for the changes in stresses experienced by the polymer. However, the force involved in parallel demolding of large patterns was excessive and hence impractical for applications. Peel demolding (Yeo et al. 2005) (Fig. 1d) for a mold with an aspect ratio of 14 was subsequently explored, whereby a displacement-controlled load was applied to a pre-crack area at the polymer-to-mold interface. Peeling was carried out subsequent to the curing of the polymer. In our previous work, both parallel and peel demolding simulations have been based on the assumption of linear elastic polymer material properties. However, these UV polymers typically have stress-strain behavior that is non-linear (or hyperelastic) (see Fig. 2—experimental data) and demolding based on non-linear material properties would be more realistic. Numerical simulation of demolding with non-linear materials properties has not been reported. A related matter of significant interest that was not pursued in our prior work (Chan-Park et al. 2003b) is the way in which the optimal shrinkage (or, equivalently, degree of crosslinking) for effective demolding varies with the aspect ratio of the mold features.

This report presents our new demolding simulation methodology based on non-linear elastic polymer material properties. Non-linear numerical analysis was conducted to trace the stress evolution during the demolding process, which was simulated with rate independent cohesive zone modeling. Equivalent thermal strain was employed to represent shrinkage. Displacement controlled peel

Table 1 Composition mix of PUR compound

Chemical	Trade name	Supplier	Weight composition (%)
Aliphatic urethane diacrylate	EBECRYL 270	UCB Chemicals	68
Dipropylene Glycol Diacrylate (DPGDA)	SR508	Sartomer Chemicals	20
Trimethylolpropane Triacrylate (TMPTA)	SR351H	Sartomer Chemicals	10
Acrylated Silicon 3	EBECRYL 350	UCB Chemicals	2
2,2-dimethoxy-2-phenylacetophenone	Irgacure 651	Ciba Chemicals	0.2

demolding was applied subsequent to the UV curing of the polymer. Global maximum principal stress and strain energy within the polymer were used to determine the optimum shrinkage level. The effect of aspect ratio on the optimum degree of shrinkage was explored by examining two high aspect ratios (5 and 10). Some computation difficulties were encountered in the form of simulation termination or breakdown before completion of demolding. The modeling of cohesive elements involves progressive damage, leading to softening in the interface element material response, and therefore, numerical instabilities when delamination was about to occur. In order to work around the non-convergent issues, the load steps used were adjusted and the simulation would be restarted from the last step in which the numerical difficulties had not yet set in.

2 Determination of material constants for numerical modeling

2.1 Stress–strain behavior of polyurethane diacrylate

Experiments were performed to determine the basic material properties of the polymer to be simulated. The polymer of interest is formed from a polyurethane diacrylate-based oligomer. Polyurethane diacrylate was selected due to its biocompatibility and high structural rigidity, properties which could be useful in micro-fluidics or tissue engineering applications. Other additives used for the formulation include Dipropylene Glycol Diacrylate (SR508), which served as a crosslinker. Trimethylolpropane Triacrylate (SR351H) was used as a diluent. An acrylated silicone (EBECRYL 350) was added to enhance the anti-stick properties while 2,2-dimethoxy-2-phenylacetophenone (Irgacure 651) was used as the UV cure photoinitiator. The weight compositions of the individual components are listed in Table 1. The polymer recipe used has previously been successfully used in high aspect ratio UV embossing over large areas (Zhou and Chan-Park 2005). All constituents were measured by weight proportions, placed in a dark glass bottle and stirred using a magnetic stirrer for 48 h at 60°C before use.

Polyurethane diacrylate formulation (PUR) was cast on flat glass molds with peripheral spacers and UV irradiated with a mercury lamp (Karl Suss MicroTEC, model MA6) having wavelength of 365 nm and intensity 10mW/cm^2 for 30 s. The cured polymer film was then removed from the mold and refrigerated for 48 h at 4°C for quenching to prevent further dark polymerization (Kilambi et al. 2007). The resulting films had an average thickness of 250 ± 20 μm. Dumbbell sized specimens following the dimensions of ASTM standards (ASTM Standards D638-03 2003), Type V design, were punched out using a stainless steel cutter purchased from Dumbbell Co., Ltd (Model: SDMK-100-D). The specimens were placed in a dry box for 24 h before testing.

Simple uniaxial tension tests were conducted. A universal Instron testing machine, frame model 5565 with a 50 N load cell was used to conduct the tests at an extension rate of 0.01 mm/s. Figure 2 shows that the average stress-strain behavior ($n = 3$) exhibited by PUR is non-linear and hyperelastic. The average UTS of the polymer at 30% fracture strain is 5.7 MPa.

2.2 Hyperelastic material model

The commercial finite element (FE) package ABAQUS Standard version 6.4-3 (ABAQUS 2004) was used for all the numerical simulations. PUR was modeled as a general incompressible elastomer with non-linear material properties. By curve fitting the uniaxial tensile test data obtained from Sect. 2.1 to an Ogden strain energy potential (Eq. 1 below) (Ogden 1972), a hyperelastic material model was generated and the model matches the data very well. Large strain theory was used in the simulation.

$$W_U = \sum_{i=1}^{N} \frac{2\mu_i}{\alpha_i^2}\left(\bar{\lambda}_1^{\alpha_i} + \bar{\lambda}_2^{\alpha_i} + \bar{\lambda}_3^{\alpha_i} - 3\right) \quad (1)$$

$$\mu_0 = \sum_{i}^{2} \mu_i \quad (2)$$

$$\upsilon = \frac{3K_0/\mu_0 - 2}{6K_0/\mu_0 + 2} \quad (3)$$

In Eq. 1, W_U is the Ogden strain energy potential, $\bar{\lambda}_i$ are the deviatoric principal stretches. N, μ_i and α_i are material

Table 2 Coefficients in Ogden strain energy potential: μ_i, α_i

i	μ_i	α_i
1	−83.02	−3.51
2	42.37	−2.918
3	51.78	−6.15

parameters. K_0, the initial bulk modulus, was assumed to be close to infinity. In Eq. 2, μ_0 is the initial shear modulus. In Eq. 3, υ, is the Poisson ratio, based on the ratio of K_0/μ_0 and was close to 0.49995 (ABAQUS 2004) Hence, it is reasonable to assume that the PUR was almost incompressible. Table 2 shows the coefficients used in the Ogden strain energy potential (1) to approximate the experimental non-linear hyperelastic material behavior (Fig. 2).

2.3 Linear elastic material model

The linear elastic assumption for polymer material response, employed in our prior paper, significantly reduces the computational effort. To examine the differences between the linear and non-linear models, a pseudo constant linear elastic modulus of 29 MPa (Fig. 2, circled trend) was used to simulate the behavior of the cured PUR. The value of 29 MPa approximates the initial measured stiffness of the cured PUR. However, by examining the difference between linear elastic and non linear elastic material models, it was palpable that the assumption of linear material properties could lead to significantly different results as compared to the actual non-linear model. The Poisson ratio ν for the elastic model was set to be almost incompressible, at a value of 0.49995.

2.4 Defining the cohesive element

User-defined rate-independent polynomial function cohesive elements from GKSS (Scheider 2001) were used to simulate the polymer-mold interface. Figure 3 shows the Scheider traction separation curve that defines stress experienced by the cohesive elements used in the model. The interface toughness or cohesive energy Γ_0 is defined in (4) and the maximum separation δ_0 is defined in (5). Γ_0 is assumed to have a low value of 0.1 J/m^2. (δ_1/δ_0) and (δ_2/δ_0) are normalized separations (Fig. 3) This is a representative value for nickel molds coated with anti-stick compound to lower their surface energy (Chan-Park et al. 2003a). The initial portion of the curve is defined by (δ_1/δ_0) for which a small value of 0.01 was adopted. The softening branch of the curve was characterized by (δ_2/δ_0) and the value was set to be 0.75. Both values were used to minimize convergence difficulties during the numerical simulations. σ_0 is the maximum fracture strength which corresponds to the flat region of the curve between (δ_1/δ_0) and (δ_2/δ_0). At fractional separations beyond (δ_2/δ_0) the polymer experiences decreasing stresses. σ_0 is assumed to be 50% of the UTS of the polymer.

$$\Gamma_0 = \sigma_0\delta_0\left[0.5 - \frac{1}{3}\left(\frac{\delta_1}{\delta_0}\right) + 0.5\left(\frac{\delta_2}{\delta_0}\right)\right] \tag{4}$$

$$\delta_0 = \frac{2\Gamma_0}{\sigma_0}\left[1 - \frac{2}{3}\left(\frac{\delta_1}{\delta_0}\right) + \left(\frac{\delta_2}{\delta_0}\right)\right]^{-1} \tag{5}$$

Mixed mode fracture behavior (Modes I and II) was assumed in the model. Parameters for Mode I and Mode II were assumed to be similar. The failure criterion for cohesive zone modeling was determined by the interface energy. When the interface energy of the interface element exceeded Γ_0, the element was reckoned to have delaminated. The UTS of the polymer was used as a failure criterion. When the maximum principal stress experienced by the polymer was greater than UTS of the cured polymer, the polymer was reckoned to have fractured prematurely and demolding was considered to have failed.

3 Finite Element Modeling

When multifunctional photocurable resins polymerize, crosslinks are formed due to the conversion of double bonds. Varying the UV intensity and/or time will change the degree of thermoset shrinkage and the polymer mechanical properties such as brittleness and cohesive strength which will strongly influence the outcome of demolding. The shrinkage that attends crosslinking facilitates demolding. But an excessively brittle polymer, one that is

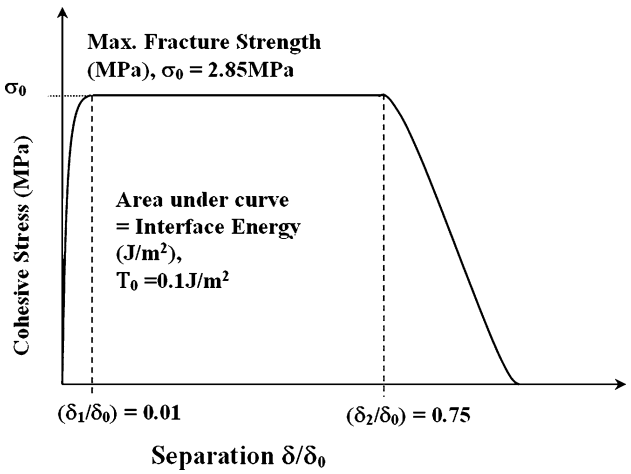

Fig. 3 A tri-linear traction separation Scheider curve in which maximum fracture strength is set at 2.85 MPa and the cohesive energy, Γ_0, at 0.1 J/m^2

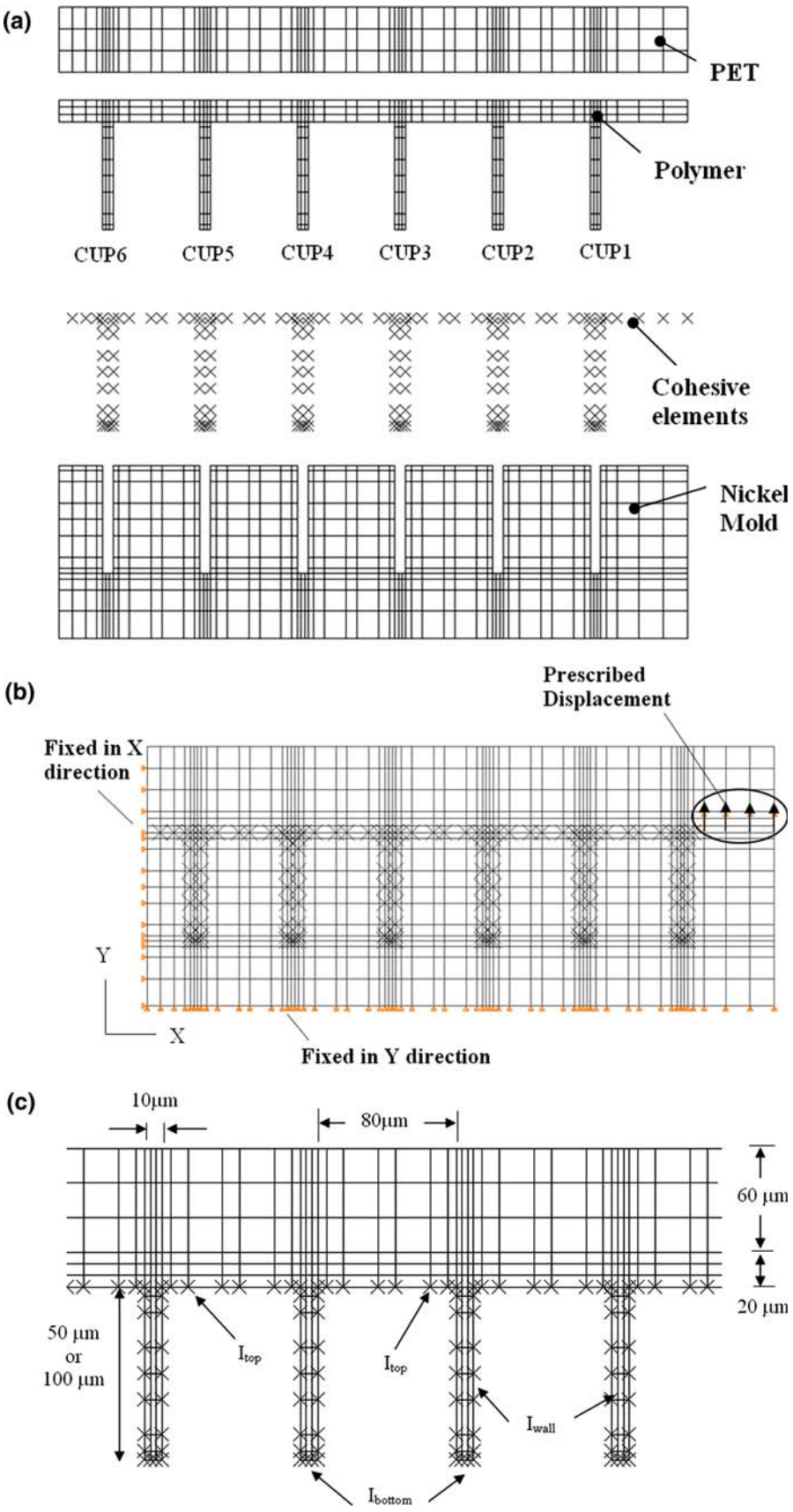

Fig. 4 Finite Element models **a** PET-polymer-cohesive elements-mold assembly. Cup 1–Cup 6 are labeled consecutively from right to left, **b** Boundary conditions and prescribed displacement (↑) shown in assembled model. Prescribed displacement was applied at highlighted ellipse with pre-crack incorporated (by removing the cohesive elements after shrinkage is completed). **c** Dimensions of PET film, polymer, trench width, spacing and depth are noted. Cohesive elements are denoted by (X). The labels I_{top}, I_{wall} and I_{bottom} denote the distinct interface regions in which cohesive element delamination must take place during demolding

Table 3 Material properties of PET and nickel

Material	Elastic modulus (GPa)	Poisson ratio
PET film	4.4	0.33
Nickel mold	200	0.33

too extensively crosslinked, is vulnerable to fracture during demolding, spoiling the mold as well as the molded object. Insufficient crosslinking, on the other hand, may result in a polymer that has shrunk too little to significantly facilitate demolding and that also has too little cohesive strength to sustain the stresses of demolding, again spoiling the mold and the molded object. Between the limits of inadequate and excessive crosslinking (and the corresponding degrees of shrinkage) there may, for any given formulation, be a range of degrees of crosslinking that permit demolding with little or no marring of the molded object. Within this range, there will be an optimal degree of crosslinking,

Several assumptions were made to render the modeling tractable. UV embossing is typically an isothermal process; consequently, shrinkage was represented as pseudo equivalent thermal strain for analysis purposes. It was assumed that the polymer behaved as a perfectly hyperelastic material. Hysteresis effects and sliding friction forces were assumed to be negligible. The stress-strain data for a nominal UV cure time of 30 s was used throughout the modeling process. The polymer replication is assumed to have taken place within a rigid nickel mold of the kind that can be fabricated with micromachining and nickel electroforming methods (Agarwal et al. 2005).

The finite element model consists of a rigid nickel mold, the replicated crosslinked polymer and a thin substrate layer of Polyethylene Terephthalate (PET) film. The PET film and polymer were modeled such that no delamination would occur. Figure 4a shows the finite element model as separate material entities for clearer visualization. For ease of simulation and without loss of generality a plane strain assumption was employed. 2D plane strain hybrid elements CPE4H were used to model the substrate film PET-polymer-mold assembly. As a representative model, 6 microwalls, denoted Cup 1 to Cup 6 from right to left were simulated. The PET and nickel mold were modeled as isotropic elastic materials, with their material properties shown in Table 3. The material properties of the cohesive elements are as described in Fig. 3. PET-polymer interface was modeled as a continuous interface such that no separation would occur since in actual experiments, the polymer bonded well to the surface-treated PET film.

Figure 4b shows the assembled mode of the finite element model with boundary and loading conditions. The rigid mold was fixed in the X direction at the left vertical

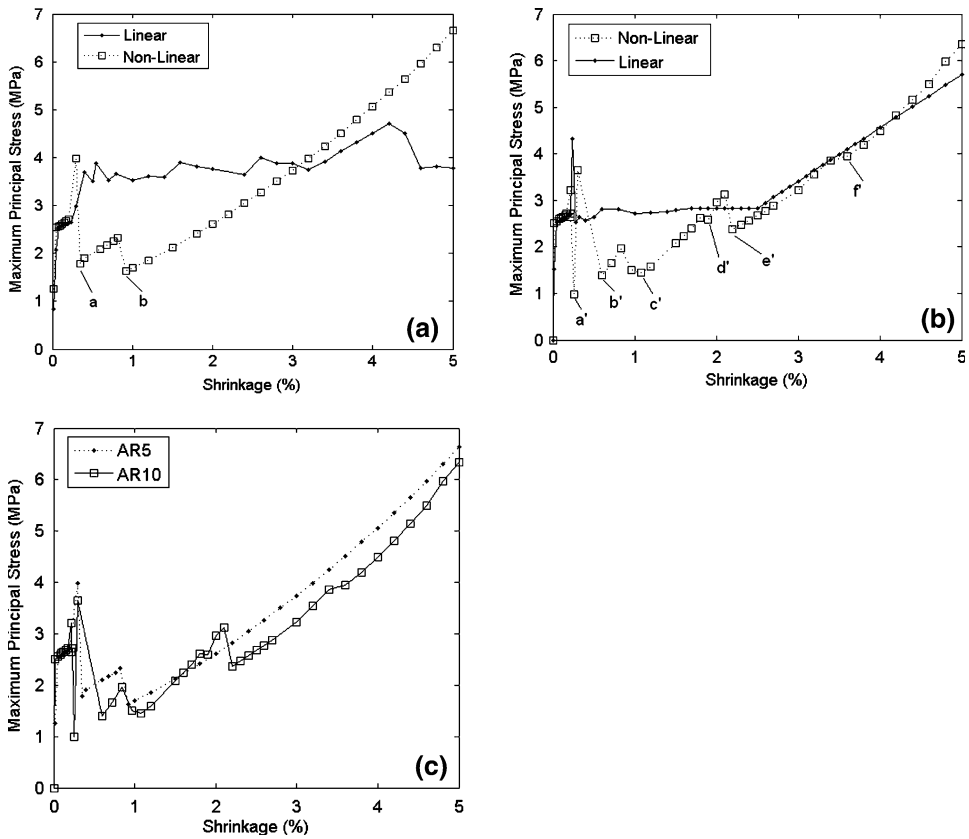

Fig. 5 Computed maximum principal stress versus shrinkage using linear and non-linear polymeric material properties at **a** AR 5, **b** AR 10, **c** both AR5 and AR10 with only non-linear model. Points a, b, a′, b′, c′, d′, e′ and f′ were identified as indications that an interface had delaminated based on a drop in global maximum principal stresses in the AR5 and AR10 non-linear models

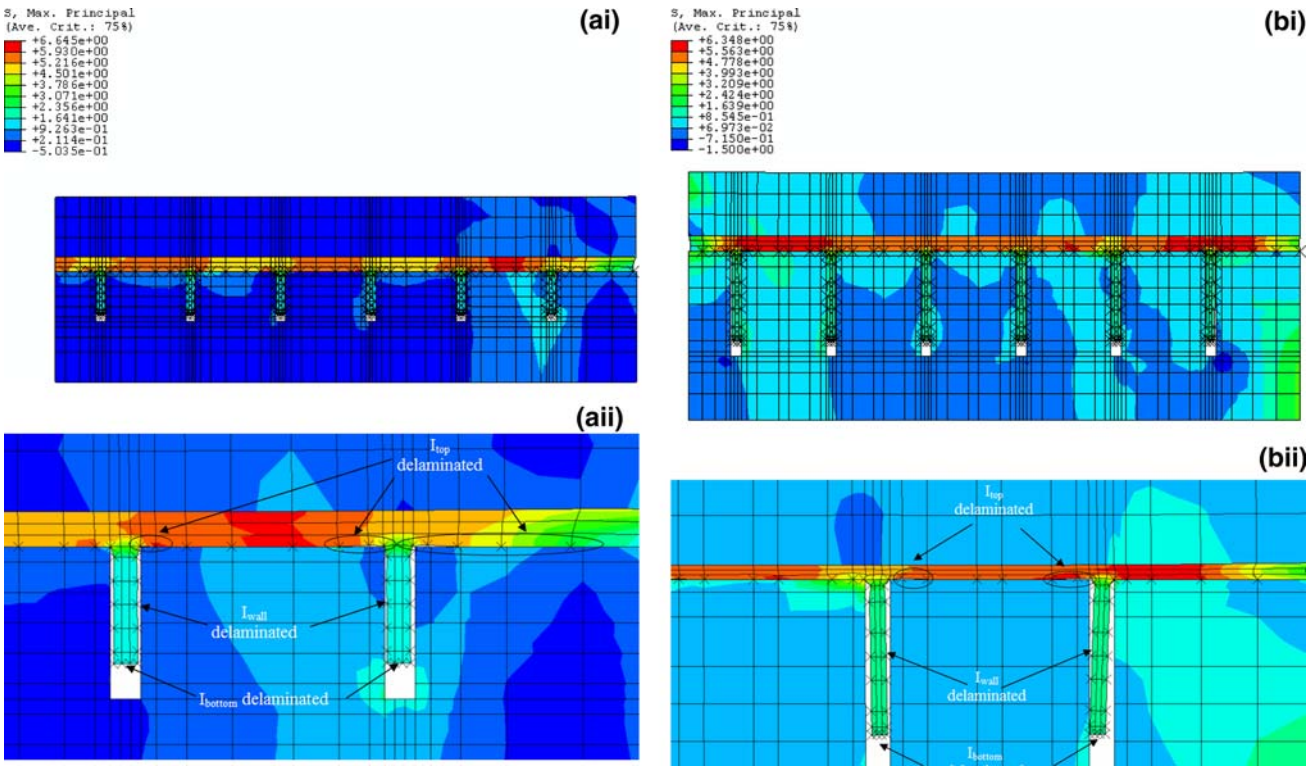

Fig. 6 Maximum principal stress contour plot at shrinkage level 5% for non-linear elastic polymer material behavior **a**i AR5 Full model, **a**ii AR5—Cups 1 and 2 at Deformation Scale 3, **b**i AR10 Full model, **b**ii AR10—Cups 1 and 2 at Deformation Scale 5

surface and in the Y direction at the bottom surface. Shrinkage represented by equivalent thermal strain in the model was applied to the polymer. By setting a coefficient of thermal expansion of 0.1E-3/°C, a shrinkage value of 5% (which was the maximum shrinkage possible for polyurethane diacrylate compound determined experimentally (Yeo 2008) could be easily simulated by setting a pseudo temperature change of −500°C to the polymer. It should be noted that this temperature change and the coefficient of thermal expansion are not physical; they are imposed to induce strain in the model that corresponds to the shrinkage-induced strain experienced by a real micromolding that is contacted to its mold and has undergone crosslinking. A pre-crack between the polymer and the mold experimentally achieved by a knife incision at the polymer-mold interface after the completion of shrinkage was simulated by removing some interface elements (Fig. 4b, eclipse area). Then an increasing prescribed displacement load was applied to the corner of the polymer at the pre-crack corner.

Figure 4c illustrates the dimensions of the finite element model. Trench width and spacing of 10 and 80 μm respectively, were assigned. The thickness for PET film and Polymer were 60 and 20 μm, respectively. The simulated array depth of 50 and 100 μm corresponded to an aspect ratio of 5 and 10. Trench width and spacing were kept constant for all aspect ratios. The labels I_{top}, I_{wall} and I_{bottom} denote the distinct regions of cohesive element delamination.

Numerical convergence was more difficult to obtain in the higher-aspect-ratio simulations. This was most likely due to the larger number of cohesive elements embedded between the hybrid plane strain elements used to model the rest of the materials. Poor convergence was also common in models that were analyzed with shrinkage levels less than 1%. A possible reason for this instability could be the rapid increase of the stress on the interface elements with displacement in the initial stiffening branch of the traction-separation curve (See Fig. 3).

Both linear and non-linear elastic polymer material behaviors were investigated for all shrinkage loads up to 5% shrinkage for aspect ratios of 5 and 10 to assess the difference between the stress evolutions in of the different aspect ratio demoldings. To determine the desired shrinkage level at aspect ratios 5 and 10, for the non-linear elastic material models, simulations were performed based on selected shrinkage levels. These levels were determined as the shrinkage levels that the interface had delaminated based on the global maximum principal stress and also intermediate shrinkage levels of 2, 3 and 4%. For abbreviation, the models are named as ARX, whereby AR means Aspect Ratio; X is either 5 or 10.

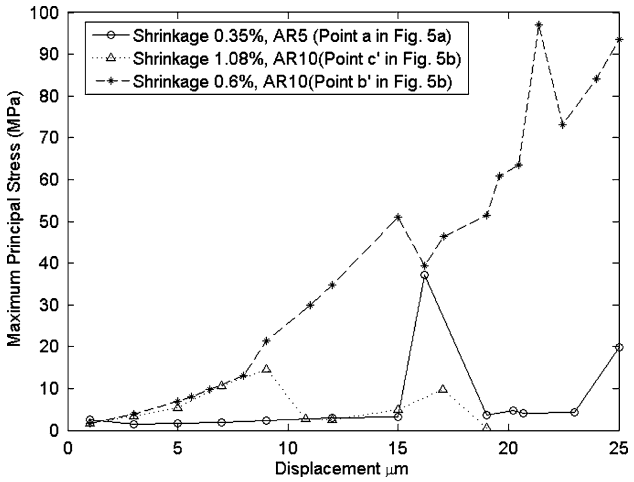

Fig. 7 Plots of maximum principal stress versus displacement at different shrinkage levels. Abnormally high stresses were recorded, indicating the occurrence of numerical difficulties

4 Results and Discussion

4.1 Shrinkage load only

Figure 5 compares the global maximum principal stresses experienced by the polymer at various shrinkage levels (%) using linear elastic and non-linear elastic polymer material properties for both AR5 and AR10. A shrinkage level of up to 5% was investigated. Significant difference in the stresses is evident between the non-linear and linear elastic polymer material properties. In general, we would expect the overall stresses to be lower using the non-linear elastic model since the modulus decreases as the polymer approaches fracture (Fig. 2). However, as shrinkage progresses, the responses of the interface elements (*i.e.* delamination) between linear and non-linear elastic material models were different due to different stress evolution history. Due to this different delamination behavior, the overall stresses could be higher for the non-linear elastic model than that of the elastic model, at the same shrinkage level.

Interface delamination can be detected by sudden decrease in the maximum principal stress versus shrinkage plot (*e.g.* Points a and b in Fig. 5). An interface delamination causes a loss of integrity and stiffness of the structure. For displacement loading, this will cause a sudden decrease in the maximum principal stress for a given displacement load. This delamination is captured by the typical cohesive element behavior. Subsequent to delamination, the interface energy of the element is expanded with no stress across the element. Further separation will result in no stress transferred across the interfacial element.

For AR5, using the non-linear stress model, noticeable interface delamination occurred at two distinct shrinkage levels of 0.35% (Point a) and 1% (Point b) as indicated in the maximum principal stress vs. shrinkage plot (Fig. 5a). The stresses started to ascend between shrinkage levels of 1% to 5%, indicating that no cohesive interface element had delaminated. Using the linear elastic material property model, the maximum principal stress between the shrinkage levels of 0.4% to 3.2% showed only slight increase and then decrease, with decreases indicative of interface element fracture. This appeared to be indicative that interface element delamination was occurring throughout the span of shrinkage level between 0.4% to 3.2%. Between the shrinkage levels of 3.2% to 4.2%, the stresses increased but decreased after interface delamination took place at 4.2% shrinkage.

As for AR10 (Fig. 5b), interface delamination occurred at shrinkage levels of 0.26% (Point a'), 0.6% (Point b'), 1.08% (Point c'), 1.9% (Point d'), 2.2% (Point e') and 3.6% (Point f') for the non-linear elastic material property model. Beyond 2.2% shrinkage level, the maximum principal stress appeared to increase with increasing shrinkage levels (except at 3.6%). The stresses for linear elastic material model between shrinkage levels 0.6% to 2.5% appeared to be constant, indicating no failure of any cohesive interface element. Beyond 2.5% shrinkage level, the stresses for linear elastic material model also increased with increasing shrinkage loads.

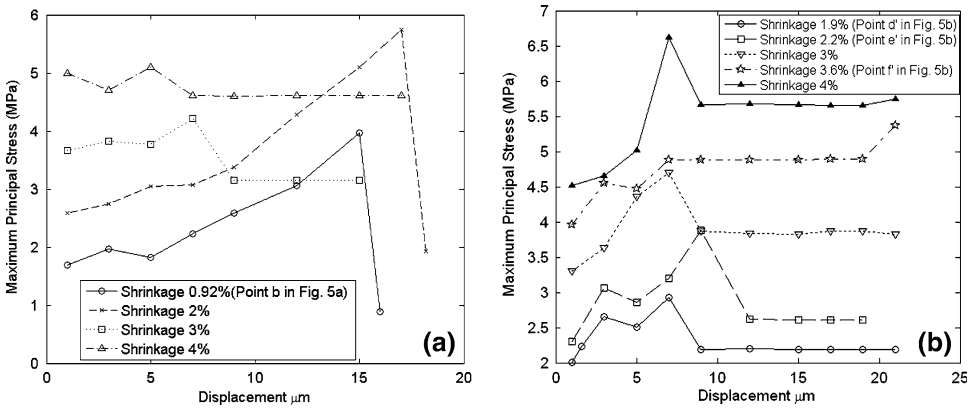

Fig. 8 Maximum principal stress (MPa) versus Displacement (μm) for **a** AR5, **b** AR10 at various Shrinkage levels

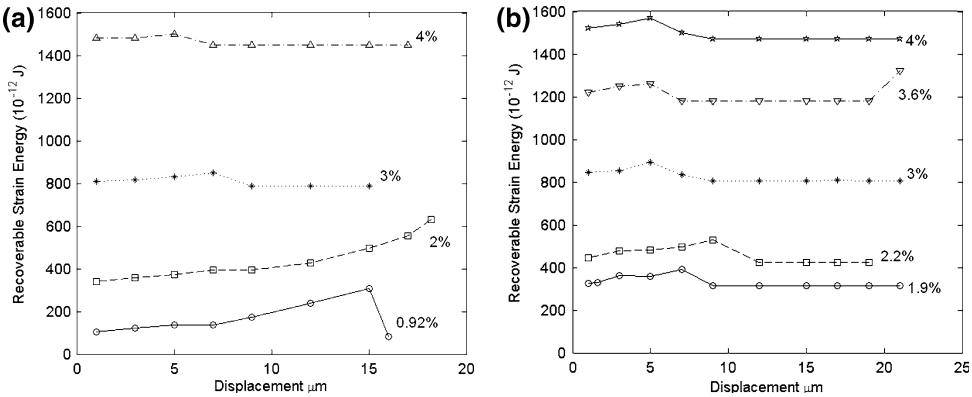

Fig. 9 Recoverable Strain Energy (10^{-12} J) versus Displacement (μm) at different shrinkage levels for **a** AR5, **b** AR10

Comparison of the linear and non-linear material properties results in Fig. 5a and 5b indicates that although linear elastic polymeric material behavior simplified computation, it could only indicate trends for preliminary study. For more realistic predictions, non-linear material behavior had to be employed. Only non-linear material behavior is considered in all subsequent discussions unless specified otherwise.

Figure 5c plots the maximum principal stresses for non-linear polymer material property vs. shrinkage levels for both AR5 and AR10. For all aspect ratios, applying a maximum shrinkage level of 5% was far from ideal since the maximum principal stresses would have exceeded the UTS of the polymer, 5.7 MPa. Based on the results shown in Fig. 5c, the UTS threshold was exceeded at shrinkage levels 4.4% (5.7 MPa) and 4.7% (5.75 MPa) for AR5 and AR10, respectively.

Interface material properties were kept similar for both aspect ratios, with δ_0 specified to be 0.045 μm for both Modes I and II fracture. The shrinkage levels at which interface delamination started to occur were compared. At the lower aspect ratio (AR5), slightly higher shrinkage loads were required before the interface started delaminating. For the higher aspect ratio, the trench is deeper and this lowered the overall thermal strain threshold for delamination along the wall region. Hence delamination initiated at lower shrinkage levels for the interface elements along the I_{wall} region. In addition, for higher aspect ratio, the polymer experiencesd more constraints hence higher stresses were experienced and consequently more interfaces delaminated. For AR5, interface delamination based on global maximum principal stress plots occurred at shrinkage levels 0.35% and 0.92%.

The typical interface delamination behavior for AR10 is illustrated in Fig. 5b. At point a′ (shrinkage level 0.26%), all I_{bottom} interfaces have delaminated except some at Cup 1. For point b′ (shrinkage level 0.6%), I_{wall} interfaces for all Cups had delaminated. At shrinkage level 1.08% (point c′), all I_{bottom} have broken. Point d′, corresponding to shrinkage level 1.9%, recorded an increase in the number of I_{wall} interfaces delaminated. Finally, for points e′ and f′ (shrinkage 2.2% and 3.6%), I_{top} interfaces near the corners of Cups 1 and 2 started to break.

Figure 6 shows the maximum principal stress contour plots at 5% shrinkage level for AR5 and AR10, respectively. In general, the interface at I_{bottom} delaminated first followed by I_{wall}. Shrinkage alone caused more delamination at the I_{top} interfaces for lower aspect ratio (AR5) (Fig. 6a) than for aspect ratio 10 (Fig. 6b). At shrinkage level 5%, for AR 5, all of I_{bottom} and I_{wall} interfaces delaminated. The I_{top} interfaces around Cup 1 and some of Cup 2 delaminated (highlighted by the ellipses in 6a-ii). For AR 10, all the I_{bottom} and I_{wall} have demolded with very few I_{top} demolded at the corners perpendicular to I_{wall}. As shown in Fig. 6, at a shrinkage level of 5%, the maximum principal stresses have exceeded the UTS of 5.7 MPa of the polymer, indicating that some premature fracture of the polymer would have taken place.

4.2 Shrinkage and displacement controlled load

Shrinkage alone could not break all the interfaces. For the polymer to demold completely, an externally applied load was required at the edge (Fig. 4b whereby prescribed displacement was applied at the highlighted eclipse area). An incremental displacement-controlled load was modeled for improving computational stability, and it was further assumed that a pre-crack had been created at the edge of the polymer. When the displacement-controlled load was

Table 4 Summary of optimum shrinkage level at different aspect ratios and the corresponding maximum principal stresses and maximum strain energy released

Aspect ratio	Shrinkage (%)	Maximum principal stress (MPa)	Maximum strain energy (10^{-12} J)
5	0.92%	3.96	308.29
10	1.9%	2.92	389.88

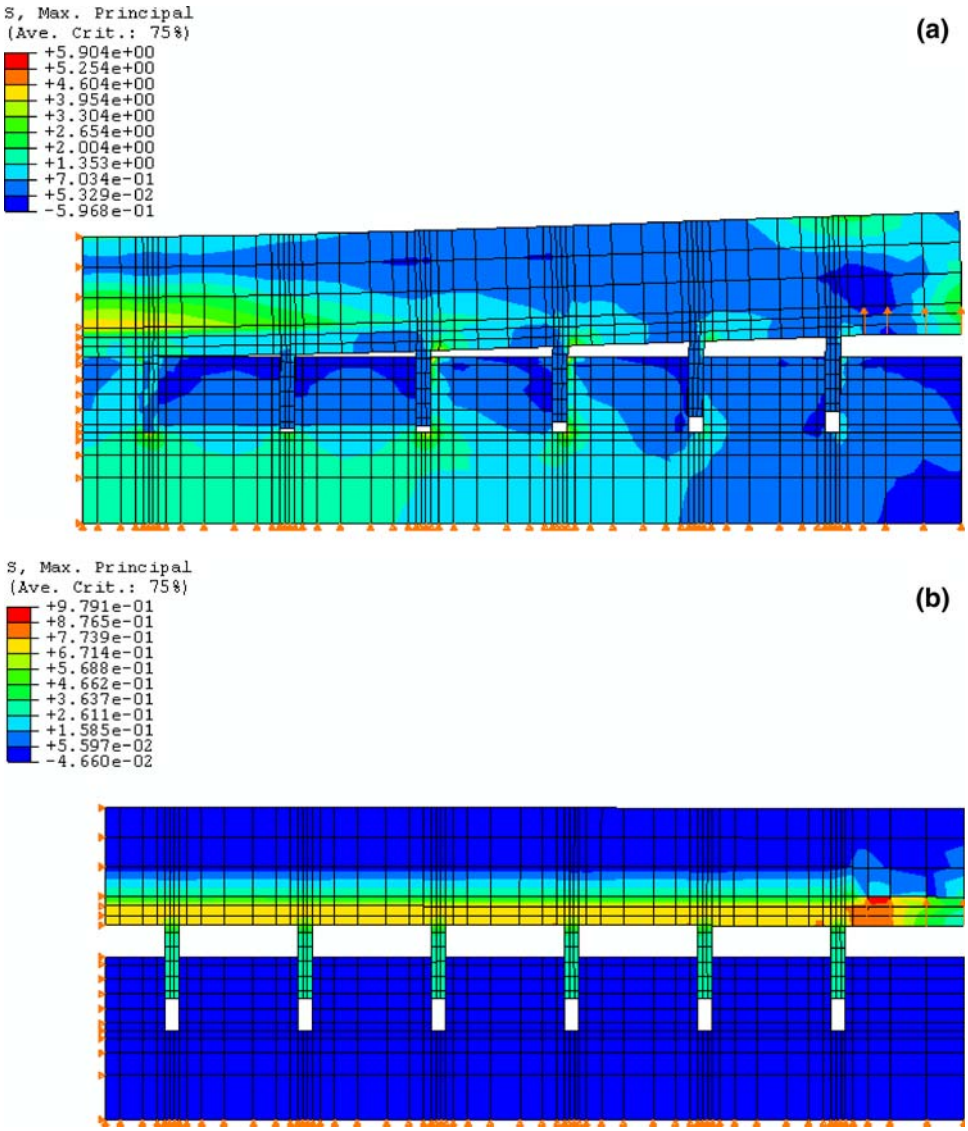

Fig. 10 Maximum principal stress contour plots for AR5 at shrinkage level 0.92% **a** before complete demolding, **b** after complete demolding

applied to models with low shrinkage levels less than 1% or slightly more than 1% (0.35% for AR5 and 0.6% and 1.08% for AR10), numerical errors were encountered. The stresses involved were extremely high ($\gg$5.7 MPa) and it was not possible to complete the simulation run for all 6 Cups in the array. This behavior was expected since at low shrinkage levels, few cohesive elements had delaminated and the polymer had to overcome higher stresses to achieve demolding. Figure 7 shows the stress history for peel demolding that occurred at various low shrinkage levels for AR5 and AR10. Abnormally high stresses were encountered and these indicated that numerical errors had occurred due to the numerical instability experienced when the cohesive elements were about to delaminate. Shrinkage level 0.35% at AR5, 0.6 and 1.08% at AR10, corresponding to points a in Fig. 5a, and b' and c' in Fig. 5b showed erroneous stress history due to convergence problems (Fig. 7).

4.3 Optimum shrinkage load

Shrinkage is an aid to demolding since the polymer tends to "pull" away from the mold after UV irradiation, reducing the polymer/mold interaction forces that must be overcome in demolding. As the cross-linking density increases with longer UV irradiation time or dosage, the rigidity of the network formed also increases, resulting in higher polymer strength. However, higher elastic modulus comes at a price of increased brittleness and too much shrinkage also results in the loss of dimensional fidelity during replication. There is an optimal degree of crosslinking and associated shrinkage, which it is desirable to determine.

For our application, the optimum shrinkage load is defined as the shrinkage level that results in the lowest recoverable strain energy and lowest maximum principal stress found globally in the polymer as a prescribed displacement was applied. Since there was no plastic work

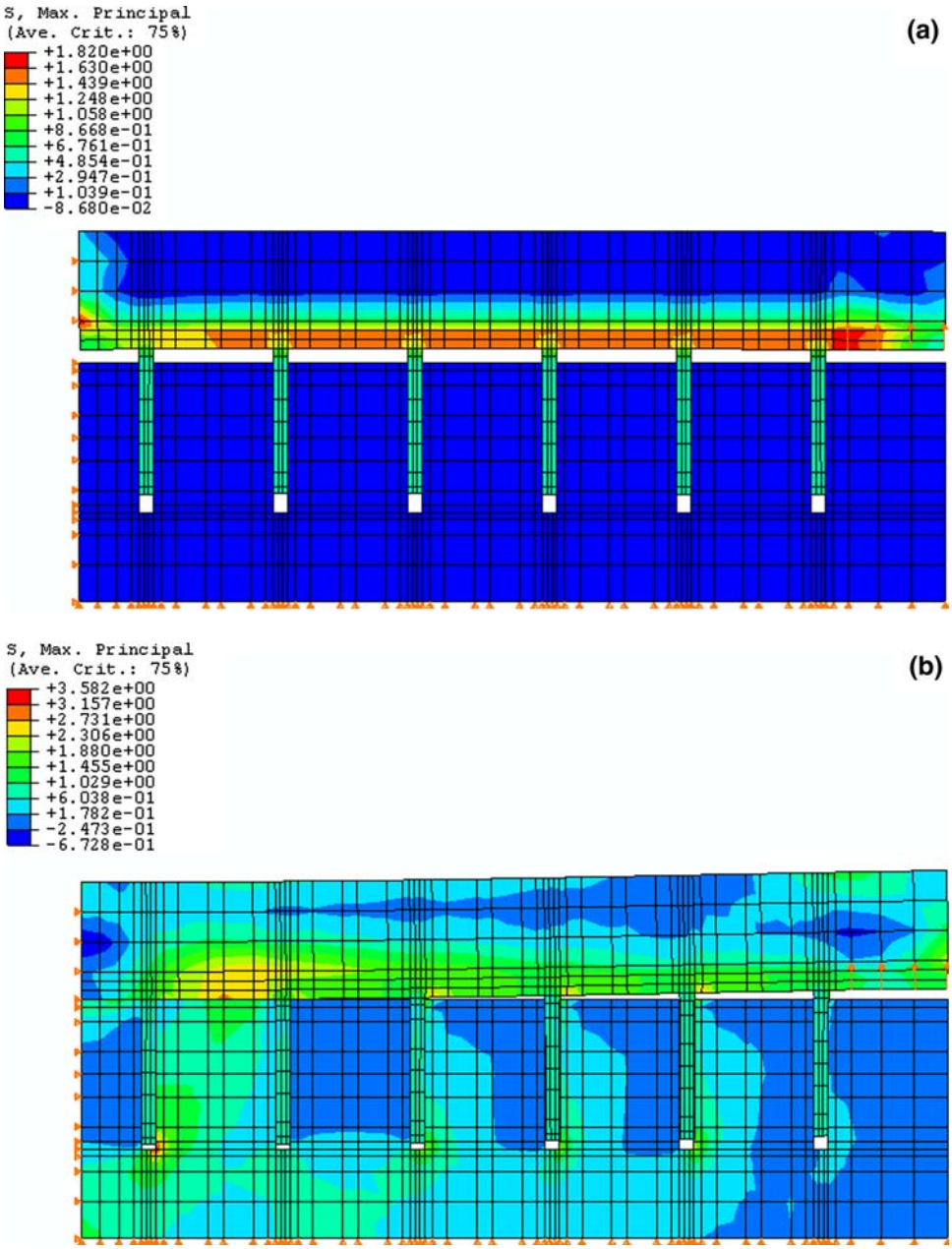

Fig. 11 Maximum principal stress contour plots for AR10 at shrinkage level 1.9% **a** before complete demolding, **b** after complete demolding

done, the recoverable strain energy derived was the elastic work stored in the polymer due to peel demolding, and it indicated the level of work done to demold. Polymer premature failure behavior was not reflected as the data presented was the overall energy. The premature failure could be reflected by the maximum principal stress during the demolding process. Previously, one of the failure criteria stated was that if the maximum principal stress exceeded the polymer UTS, polymer fracture would have occurred. However, from the maximum principal contour plots shown, the high maximum principal stress was at the occurrence of numerical convergence difficulties. It was hence reasonable to assume that these were not actual fracture points since the stresses would have redistributed with delamination or yielding.

Specific shrinkage loads at which an interface had delaminated, identifiable through the decrease and then increase in global maximum principal stresses as seen in Fig. 5c, were selected for analysis. Intermediate shrinkage levels of 2%, 3% and 4% were also investigated. Figure 8 shows the maximum principal stress in the polymer versus displacement and Fig. 9 shows the corresponding recoverable strain energy versus displacement for both AR5 and AR10 after the shrinkage load was completed. The

optimum shrinkage level for AR5 and AR10 based on the various shrinkage levels investigated were found to be close to 0.92 and 1.9%, respectively. The values were determined based on the lowest maximum principal stresses and lowest recoverable strain energy at a specific shrinkage level. From an experimental perspective, proper design of experiments can be carried out to obtain the optimum shrinkage level with a change in aspect ratio. Table 4 summarizes the results of the optimum shrinkage levels and their corresponding maximum principal stress and recoverable strain energy at various aspect ratios. Optimum shrinkage level increased with increasing aspect ratio. This conformed to our expectation since, as aspect ratio increases the difficulty to demold also escalates due to more mechanical interlocking between the polymer and the mold.

Figures 10 and 11 show the maximum principal stress contour plots at the optimum shrinkage levels for each aspect ratio at the largest prescribed displacement applied. Two maximum principal stress contour plots are shown for each aspect ratio for the step before complete demolding and the step after complete demolding was achieved. The global maximum principal stresses decreased from 5.90 MPa (before) to 0.98 MPa (after complete demolding) for the AR5 model. In theAR10 model, the stresses decreased from 3.58 to 1.82 MPa. The decrease in the stresses experienced by the polymer in both AR5 and AR10 indicate that full demolding had occurred.

5 Conclusions

A new numerical methodology which involves the use of hyperelastic polymeric material properties instead of linear elastic material properties were used during the peel demolding simulation for UV embossing. During the simulation, numerical convergence difficulties were encountered. These were overcome by employing smaller load steps to avoid the non-convergence points during the application of shrinkage and prescribed displacement loads. Shrinkage load alone was not capable of breaking all the interface elements between polymer and mold. Displacement load could be applied after the shrinkage load was completed to aid demolding. Optimal shrinkage was determined whereby the polymer experienced the lowest maximum principal stress and lowest strain energy. Based on the molds with aspect ratio 5 and 10, the optimum shrinkage load was found to be 0.92 and 1.9%, respectively.

Acknowledgements L. P. Yeo acknowledges the sponsorship of a graduate scholarship from the SMA-IMST program. This research was partially supported by an A*STAR (Singapore) grant (Project No. 042 114 0041).

References

ABAQUS (2004) Version 6.4, Theory and User Manuals I, II, III. Hibbitt, Karlsson and Sorensen, Inc., 1080 Main Street, Pawtucket, RI, 02860-4847, USA

ASTM Standard D638-03 (2003) Standard test method for tensile properties of plastics, ASTM International, West Conshohocken, PA

Agarwal M, Gunasekaran RA, Coane P et al (2005) Scum free patterning of SU-8 resist for electroforming applications. J Micromech Microeng 15:130–135. doi:10.1088/0960-1317/15/1/020

Anderson DG, Putnam D, Lavik EB et al (2005) Biomaterial microarrays: rapid, microscale screening of polymer-cell interaction. Biomaterials 26:4892–4897. doi:10.1016/j.biomaterials.2004.11.052

Bender M, Otto M, Hadam B et al (2000) Fabrication of nanostructures using a UV-based imprint technique. Microelectron Eng 57:233–236. doi:10.1016/S0167-9317(00)00304-X

Chan-Park MB, Neo WK (2003) Ultraviolet embossing for patterning high aspect ratio polymeric microstructures. Microsyst Technol 9:501–506. doi:10.1007/s00542-002-0289-0

Chan-Park MB, Gao JX, Koo HL (2003a) Surface characterization of nickel alloy plasma-treated by O_2/CF_4 mixture. J Adhes Sci Technol 17:1979–2004. doi:10.1163/156856103322584173

Chan-Park MB, Lam YC, Laulia P et al (2003b) Simulation and investigation of factors affecting high aspect ratio UV embossing. Langmuir 21:2000–2007. doi:10.1021/la035124e

Chan-Park MB, Yan YH, Neo WK et al (2003c) Fabrication of high aspect ratio Poly(ethylene glycol)-containing microstructures by UV embossing. Langmuir 19:4371–4380. doi:10.1021/la026967t

Cornec A, Scheider I, Schwalbe KH (2003) On the practical application of the cohesive model. Eng Fract Mech 70:1963–1987. doi:10.1016/S0013-7944(03)00134-6

Gale MT (1997) Replication. In: Herzig HP (ed) Micro-optics: elements, systems and applications, 1st edn. Taylor and Francis, London, pp 153–154

Gao JX, Chan-Park MB, Xie DZ et al (2004) UV embossing of submicrometer patterns on biocompatible polymeric films using a focused ion beam fabricated TiN mold. Chem Mater 16:956–958. doi:10.1021/cm0342849

Gao JX, Yeo LP, Chan-Park MB et al (2006) Anti-stick post passivation of high-aspect ratio Silicon molds fabricated by deep-reactive ion etching. J MicroelectroMech S 15:84–93. doi:10.1109/JMEMS.2005.863795

Kilambi H, Reddy SK, Schneidewind L et al (2007) Copolymerization and dark polymerization studies for photopolymerization of novel acrylic monomers. Polymer (Guildf) 48:2014–2021. doi:10.1016/j.polymer.2007.02.006

Ogden RW (1972) Large deformation isotropic elasticity-on the correlation theory and experiment for incompressible rubberlike solids. Proc R Soc Lond Ser-A A 326:565–583

Otto M, Bender M, Hadam B et al (2001) Characterization and application of a UV-based imprint technique. Microelectron Eng 57:361–366. doi:10.1016/S0167-9317(01)00536-6

Rahulkumar P, Jagota A, Bennison SJ et al (1999) Polymer interfacial fracture simulations using cohesive elements. Acta Mater 47:4161–4169. doi:10.1016/S1359-6454(99)00276-1

Rahulkumar P, Jagota A, Bennison SJ et al (2000) Cohesive element modeling of viscoelastic fracture: application to peel testing of

polymers. Int J Solids Struct 37:1873–1897. doi:10.1016/S0020-7683(98)00339-4

Scheider I (2001) Cohesive model for crack propagation analyses of structures with elastic-plastic material behavior: foundations and implementation. GKSS research center Geesthacht, Dept. WMS

Shvartsman FP (1991) Holographic optical elements by dry photopolymer embossing. Proc SPIE 1461:313–320. doi:10.1117/12.44742

Unger MA, Chou HP, Thorsen T et al (2000) Monolithic microfabricated valves and pumps by multilayer soft lithography. Science 288:113–116. doi:10.1126/science.288.5463.113

Xu XP, Needleman A (1994) Numerical simulations of fast crack growth in brittle solids. J Mech Phys Solids 42:1397–1434. doi:10.1016/0022-5096(94)90003-5

Yeo LP (2008) Demolding mechanics of micro-cast UV thermosets. Ph.D. Nanyang Technological University, Singapore

Yeo LP, Lam YC, Chan-Park MB et al (2005) Demolding of high aspect ratio polymeric micro-patterning. Int J Nanoscience 4:543–549. doi:10.1142/S0219581X05003462

Zhou WX, Chan-Park MB (2005) Large area UV casting using diverse polyacrylates of microchannels separated by high aspect ratio microwalls. Lab Chip 5:512–518. doi:10.1039/b419330j